

Quantum tomography of a third-order exceptional point in a dissipative trapped ion

Received: 20 November 2024

Accepted: 24 July 2025

Published online: 12 August 2025

 Check for updatesY.-Y. Chen^{1,5}, K. Li^{1,2,5}, L. Zhang^{1,5}, Y.-K. Wu^{1,3}, J.-Y. Ma⁴, H.-X. Yang⁴, C. Zhang⁴, B.-X. Qi¹, Z.-C. Zhou^{1,3}, P.-Y. Hou^{1,3}✉, Y. Xu^{1,3}✉ & L.-M. Duan^{1,3}✉

Hermiticity in quantum mechanics ensures the reality of energies, while parity-time symmetry offers an alternative route. Interestingly, in a three-level system, parity-time symmetry-breaking can lead to third-order exceptional points with distinctive topological properties. Experimentally implementing this in open quantum systems requires two well-controlled loss channels, resulting in dynamics that challenges a pure non-Hermitian description. Here we address the challenge by employing two approaches to eliminate the effects of quantum jump terms, ensuring pure non-Hermitian dynamics in a dissipative trapped ion. Based on this, we experimentally observe a parity-time symmetry-breaking-induced third-order exceptional point through non-Hermitian absorption spectroscopy. Quantum state tomography further demonstrates the coalescence of three eigenstates into a single eigenstate at the exceptional point. Finally, we identify an intrinsic third-order Liouvillian exceptional point via quench dynamics. Our experiments can be extended to observe other non-Hermitian phenomena involving multiple dissipative levels and potentially find applications in quantum information technology.

Hermiticity is a fundamental concept in quantum mechanics as it ensures the reality of energies. Interestingly, it has been discovered that the requirement of Hermiticity can be relaxed in favor of considering parity-time (PT) symmetry, which also guarantees the reality of energies when the corresponding eigenstates respect the symmetry^{1–3}. Notably, if a state violates the symmetry, its eigenvalue becomes complex. In a two-level system, a second-order exceptional point (EP2) appears at the transition point, where the Hamiltonian becomes nondiagonalizable^{4,5}. The PT symmetry breaking in two-level systems has garnered significant interest across various fields, further promoting the study of diverse phenomena in non-Hermitian physics^{6–12}, including single-mode lasers^{13,14}, exceptional points, rings or knots^{15–24}, enhanced sensing²⁵, and unidirectional invisibility²⁶. Moreover, experimental observations have confirmed the existence of two-mode PT symmetry breaking and related non-Hermitian topology in quantum systems^{27–36}.

In systems with more than two levels, the PT symmetry breaking can lead to higher-order exceptional points (EPs) beyond the second order. For instance, in a ternary PT symmetric system, a third-order EP (EP3) can arise from the PT symmetry breaking, where a 3×3 non-Hermitian Hamiltonian has only one eigenstate. Remarkably, higher-order EPs can exhibit peculiar topological properties and sensitivity enhancement^{37–40}. Consequently, significant efforts have been directed towards experimentally exploring EP3 and their topological properties in optical systems^{41,42}, cavity optomechanical systems³⁹, acoustics systems⁴⁰, and Bose-Einstein condensates⁴³. In quantum systems, two approaches are usually employed to implement a non-Hermitian Hamiltonian. One approach, named the dilation method, employs the dynamics of a Hermitian Hamiltonian involving a system qubit and an ancilla qubit to realize the non-Hermitian dynamics in a subspace^{27,44,45}. This method has been utilized to observe a third-order exceptional line in a nitrogen-vacancy spin system⁴⁶. The other method

¹Center for Quantum Information, Institute for Interdisciplinary Information Sciences, Tsinghua University, Beijing, PR China. ²RIKEN Center for Emergent Matter Science (CEMS), Wako, Saitama, Japan. ³Hefei National Laboratory, Hefei, PR China. ⁴HYQ Co., Beijing, PR China. ⁵These authors contributed equally: Y.-Y. Chen, K. Li, L. Zhang. ✉e-mail: houpanyu@mail.tsinghua.edu.cn; yongxuphy@tsinghua.edu.cn; lmduan@tsinghua.edu.cn

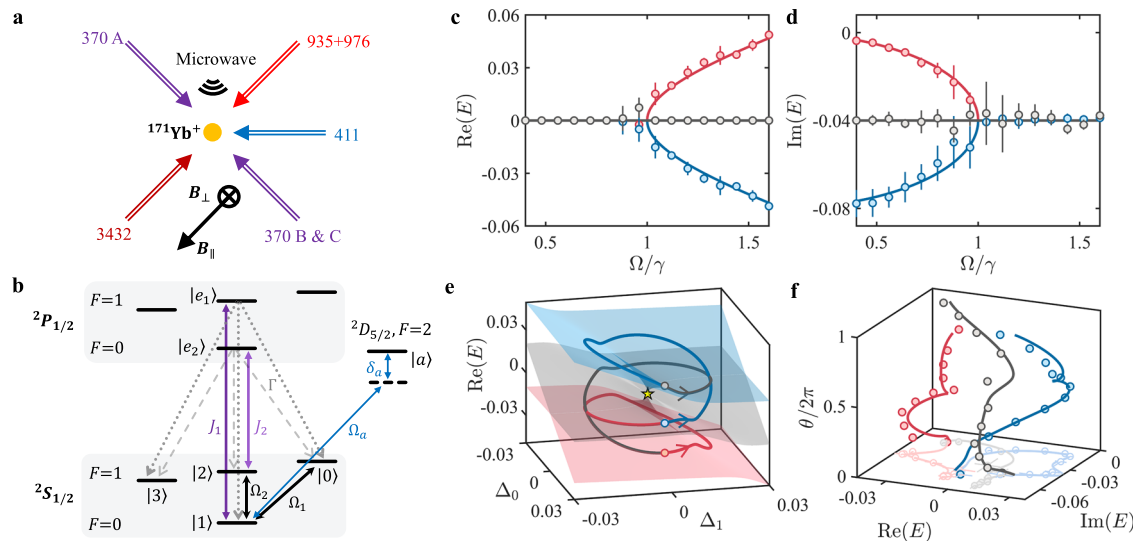


Fig. 1 | Schematics of experimental configurations, and experimental results via non-Hermitian absorption spectroscopy. **a** We use a 370 nm laser beam A for cooling, optical pumping and state detection, 370 nm lasers B and C to realize the dissipation in the $|1\rangle$ and $|2\rangle$ levels, respectively, and microwaves to generate the Hermitian part of the Hamiltonian. A 411 nm laser is applied to drive the transition between the levels $|1\rangle$ and $|a\rangle$ for non-Hermitian absorption spectroscopy. Laser with wavelengths of 935 nm, 3432 nm, and 976 nm are also utilized as auxiliary components in the experiments (see Supplementary Information S-1 for detailed descriptions of our experimental setup). The magnetic field has a small out-of-plane component in addition to the in-plane component so that $\mathbf{B} = \mathbf{B}_\parallel + \mathbf{B}_\perp$. **b** The main energy levels and transitions used in our experiment. Transitions driven by the microwaves, the 370 nm lasers B and C, and the 411 nm laser are described by black, purple, and blue arrows, respectively. Spontaneous decay of the excited states is

shown by dotted and dashed lines. Real (**c**) and imaginary (**d**) parts of complex eigenenergies obtained by theoretical calculations (solid lines) are shown together with experimental data points (circles). **e** Real part of the eigenenergies near the EP3 (marked by the star) as a function of two additional detunings Δ_0 and Δ_1 . **f** Theoretical (solid lines) and experimental complex eigenenergies (circles) with respect to θ defined through $\Delta_0 = \Delta_r \cos \theta$ and $\Delta_1 = \Delta_r \sin \theta$ with $\Delta_r = 2\pi \times 0.020$ MHz. The energy bands are marked with the same colors as in (**e**), and the starting points at $\theta = 0$ are marked by circles in (**e**). In (**c–f**) $\gamma = 2\pi \times 0.040$ MHz, $\Omega_a = 2\pi \times 0.004$ MHz, and the evolution time is $\tau_a = 200$ μ s. The experimental results are averaged over 5 rounds of experiments (each contains 200 shots) with error bars being the standard deviation of the five experimental repetitions (error bars for some data points are smaller than the symbol size).

involves applying dissipation to achieve the non-Hermitian Hamiltonian, which has been applied in cold atom systems^{28,35,43,47}, superconducting circuits^{29,30,48}, and trapped ions^{31,32,49}. However, the observation of the PT symmetry-breaking-induced EP3 in these systems requires two loss channels, making it difficult to describe the dynamics using an effective non-Hermitian Hamiltonian.

Here, we experimentally investigate the EP3 associated with PT symmetry breaking in a dissipative trapped-ion system. By precisely engineering the system Hamiltonian and two loss channels, we realize a three-level effective non-Hermitian Hamiltonian possessing both PT and anti-PT symmetries, which protect the existence of an EP3 within a one-dimensional parameter space. We prove that the dynamics in non-Hermitian absorption spectroscopy⁵⁰ is governed by the effective non-Hermitian Hamiltonian, enabling the observation of the EP3 and the associated winding topology. In particular, we find that an off-diagonal sector of a density matrix undergoes a non-Hermitian evolution, allowing us to perform quantum state tomography across the EP3. This enables the direct observation of the coalescence of three eigenstates into a single eigenstate—an unambiguous feature of an EP3. Finally, we find that the Lindbladian, which is also a non-Hermitian matrix in Liouville space, exhibits an intrinsic EP3, and we experimentally identify this EP3 by quenching a non-physical initial state.

Results

PT symmetry-breaking-induced EP3 in a dissipative trapped ion

We realize a dissipative three-level system using a single trapped $^{171}\text{Yb}^+$ ion, as illustrated in Fig. 1a. The three system levels are encoded in the hyperfine states $|0\rangle \equiv |F=1, m_F=1\rangle$, $|1\rangle \equiv |F=0, m_F=0\rangle$ and $|2\rangle \equiv |F=1, m_F=0\rangle$ within the $^2S_{1/2}$ ground state manifold (see Fig. 1b). The hyperfine splitting $\omega_{\text{HF}} \approx 2\pi \times 12.6$ GHz allows us to couple $|1\rangle$ with $|0\rangle$ and $|2\rangle$ using microwaves, as

indicated by the black arrows in Fig. 1b. To induce dissipation in $|1\rangle$ ($|2\rangle$), we use a 370 nm laser B (C) to couple it with an excited state $|e_1\rangle \equiv |^2P_{1/2}, F=1, m_F=0\rangle$ ($|e_2\rangle \equiv |^2P_{1/2}, F=1, m_F=0\rangle$), denoted by a dark (light) purple arrow in Fig. 1b. According to selection rules, $|e_1\rangle$ ($|e_2\rangle$) spontaneously decays to $|0\rangle$, $|1\rangle$ ($|2\rangle$), and $|3\rangle \equiv |F=0, m_F=-1\rangle$ with equal probabilities, as shown in Fig. 1b by the dotted (dashed) lines.

The dynamics of the system is described by the following master equation ($\hbar=1$) (see “Methods” Adiabatic elimination for the master equation for details on deriving the equation through adiabatic elimination)

$$\frac{d\rho}{dt} = \mathcal{L}[\rho] = -i[H, \rho] + \sum_{\mu=1}^6 \left(L_\mu \rho L_\mu^\dagger - \frac{1}{2} (L_\mu^\dagger L_\mu \rho + \rho L_\mu^\dagger L_\mu) \right), \quad (1)$$

where $H = \frac{\Omega_1}{\sqrt{2}} |0\rangle\langle 1| + \frac{\Omega_2}{\sqrt{2}} |1\rangle\langle 2| + \text{H.c.}$ with $\Omega_{1,2}$ being the coupling strength controlled by the microwaves, $L_1 = c_1 |0\rangle\langle 1|$, $L_2 = c_1 |1\rangle\langle 1|$, $L_3 = c_1 |3\rangle\langle 1|$, $L_4 = c_2 |0\rangle\langle 2|$, $L_5 = c_2 |2\rangle\langle 2|$, and $L_6 = c_2 |3\rangle\langle 2|$ are quantum jump operators with $c_n = \sqrt{2}\gamma_n/3$, and $\gamma_n = 2J_n^2/\Gamma$ for $n=1, 2$ ($J_{1,2}$ are controlled through 370 nm lasers B and C, and $\Gamma \approx 2\pi \times 19.6$ MHz⁵¹ arising from the short lifetime of the $^2P_{1/2}$ states). If we can neglect the contribution of quantum jump terms $\sum_{\mu} L_\mu \rho L_\mu^\dagger$, then the dynamics is governed by the effective non-Hermitian Hamiltonian $H_{\text{eff}} = H - \frac{i}{2} \sum_{\mu} L_\mu^\dagger L_\mu$, which reads

$$\begin{pmatrix} 0 & \frac{\Omega_1}{\sqrt{2}} & 0 \\ \frac{\Omega_1}{\sqrt{2}} & -i\gamma_1 & \frac{\Omega_2}{\sqrt{2}} \\ 0 & \frac{\Omega_2}{\sqrt{2}} & -i\gamma_2 \end{pmatrix} \quad (2)$$

relative to the basis $\{|0\rangle, |1\rangle, |2\rangle\}$.

When $\Omega_1 = \Omega_2 = \Omega$ and $\gamma_1 = \gamma_2/2 = \gamma$, we obtain $H_{\text{eff}} = h_{\text{eff}} - i\gamma I_3$ where I_3 is a 3×3 identity matrix and $h_{\text{eff}} = \Omega S_x + i\gamma S_z$ with S_x and S_z being the spin-1 matrices. In this case, h_{eff} respects both PT symmetry, $U_{\text{PT}} h_{\text{eff}} U_{\text{PT}}^{-1} = h_{\text{eff}}$, and anti-PT symmetry, $U_{\text{APT}} h_{\text{eff}} U_{\text{APT}}^{-1} = -h_{\text{eff}}$, where

$$U_{\text{PT}} = \begin{pmatrix} 0 & 0 & 1 \\ 0 & 1 & 0 \\ 1 & 0 & 0 \end{pmatrix} \kappa, \quad U_{\text{APT}} = \begin{pmatrix} 1 & 0 & 0 \\ 0 & -1 & 0 \\ 0 & 0 & 1 \end{pmatrix} \kappa, \quad (3)$$

with κ being the complex-conjugation operator. PT (anti-PT) symmetry ensures that an eigenenergy of h_{eff} is purely real (imaginary) when the corresponding eigenstate respects the symmetry, and the set of all eigenenergies are symmetric with respect to the real (imaginary) axis when the symmetry is broken. Consequently, as we vary a system parameter Ω/γ , if the transition for both symmetry breaking occurs at the same parameter value (e.g., $\Omega/\gamma = 1$), then the eigenenergies must transition between purely real and purely imaginary values across the transition point. At this point, all three eigenenergies are zero, and an EP3 appears⁵². Indeed, by solving the eigenvalue problem, we obtain the eigenenergies of h_{eff} as $E_{\pm} = \pm \sqrt{\Omega^2 - \gamma^2}$ and $E_0 = 0$, with the corresponding right eigenstates being

$$|\psi_{\pm}\rangle = \begin{pmatrix} -\frac{\gamma \mp i \sqrt{\Omega^2 - \gamma^2}}{2\Omega}, \frac{i}{\sqrt{2}}, \frac{\gamma \pm i \sqrt{\Omega^2 - \gamma^2}}{2\Omega} \end{pmatrix}^T, \quad (4)$$

$$|\psi_0\rangle = \frac{1}{\sqrt{\Omega^2 + \gamma^2}} \begin{pmatrix} -\frac{\Omega}{\sqrt{2}}, i\gamma, \frac{\Omega}{\sqrt{2}} \end{pmatrix}^T.$$

For $\Omega > \gamma$ ($\Omega < \gamma$), the eigenenergies are purely real (imaginary), corresponding to preserved (broken) PT symmetry. Notably, at $\Omega = \gamma$, not only do the eigenenergies become degenerate, but all three eigenstates coalesce into a single state $|\text{EP}\rangle = \frac{1}{2}(-1, i\sqrt{2}, 1)$, indicating the presence of an EP3. Thus, by tuning the ratio Ω/γ , one can observe a PT transition associated with an EP3, protected by the PT and anti-PT symmetries^{52,53}.

However, the presence of quantum jump terms $\sum_{\mu} L_{\mu} \rho L_{\mu}^{\dagger}$ can cause the dynamics to deviate significantly from the pure non-Hermitian evolution described by H_{eff} . For example, 2/3 of the decayed population is returned to the system levels through the quantum jumps, which is not the case in the non-Hermitian evolution. In the following, we will employ two approaches to eliminate the effects of the quantum jump terms and experimentally detect the EP3 in H_{eff} associated with the PT symmetry breaking. Furthermore, we find that the Lindbladian \mathcal{L} , which is also a non-Hermitian matrix in Liouville space, exhibits an intrinsic EP3 at $\Omega = \gamma$. By leveraging the anti-PT symmetry of the Lindbladian, we can experimentally detect this Liouvillian EP3 by quenching a non-physical density matrix with zero trace.

Non-Hermitian absorption spectroscopy

To measure the complex eigenenergies of the effective non-Hermitian Hamiltonian, we introduce an auxiliary energy level $|a\rangle \equiv |^2D_{5/2}, F=2, m=0\rangle$, which is coupled to the system level $|1\rangle$ by a 411 nm laser (see Fig. 1b). In this setup, the Hamiltonian is modified to

$$H_{\text{NAS}} = H_{\text{eff}} + \frac{\Omega_a}{2} (|1\rangle\langle a| + \text{H.c.}) - \delta_a |a\rangle\langle a|, \quad (5)$$

where Ω_a is the Rabi frequency, δ_a is the detuning, and the involved energy levels are $|0\rangle$, $|1\rangle$, $|2\rangle$, and $|a\rangle$. We initially prepare the ion in the auxiliary state $|a\rangle$. As time evolves, the population is transferred to the system levels and subsequently dissipates to the loss state $|3\rangle$. Finally, we measure the remaining population in $|a\rangle$ with respect to the

detuning δ_a (see Methods Sec. B), which contains information of the complex eigenenergies of the system^{49,50}.

By setting Ω_a sufficiently small, the effects of the quantum jump terms become negligible, allowing the system to undergo a non-Hermitian evolution. This is because the quantum jump terms significantly affect the dynamics only when there is sufficient population in $|1\rangle$ and $|2\rangle$. However, with a small Ω_a , any population transferred to the system levels dissipates quickly to the loss state $|3\rangle$, resulting in negligible population in $|1\rangle$ and $|2\rangle$ (see “Methods” in Non-Hermitian absorption spectroscopy). As a consequence, the population in the auxiliary level at time t_a is determined by the non-Hermitian evolution

$$N_a = N_0 |\langle a| e^{-iH_{\text{NAS}} t_a} |a\rangle|^2, \quad (6)$$

where we introduce a variable N_0 to account for the state preparation and measurement error. We extract the complex eigenenergies of the system by fitting the experimental measurement results based on the theoretical population $N_{a,i}^{\text{tgt}}$ calculated from Eq. (6) with slight modifications to account for the finite lifetime (~ 7.4 ms) of $|a\rangle$ (see “Methods” in Non-Hermitian absorption spectroscopy).

To experimentally observe the EP3 associated with the PT symmetry breaking, we tune the ratio Ω/γ from 0.4 to 1.6 across $\Omega/\gamma = 1$. By measuring the remaining population in $|a\rangle$ at the end of the dynamics with respect to the detuning δ_a (referred to as a spectral line) for each ratio and fitting these spectral lines using the method presented in Methods Non-Hermitian absorption spectroscopy, we extract the complex eigenenergies with respect to Ω/γ , with the real and imaginary components displayed in Fig. 1c and d, respectively. The measured eigenenergies closely match the theoretical values, indicating the PT symmetry-broken phase for $\Omega < \gamma$ and the unbroken phase for $\Omega > \gamma$, with the EP3 occurring at $\Omega = \gamma$.

To further confirm the existence of an EP3, we probe the spectral topology associated with the EP3. We set $\Omega = \gamma$ and introduce additional detuning terms $(-\Delta_0|0\rangle\langle 0| - \Delta_1|1\rangle\langle 1|)$ in the system levels by varying the frequencies of the microwaves. As shown in Fig. 1e, the eigenenergies with respect to Δ_0 and Δ_1 exhibit a multi-sheeted structure. Starting from an arbitrary point, one needs to encircle the EP3 three times to return to the original eigenenergy (e.g., following a path defined by $\Delta_0 = \Delta_r \cos \theta$ and $\Delta_1 = \Delta_r \sin \theta$ with $\Delta_r = 2\pi \times 0.020$ MHz as shown by the solid lines in Fig. 1e), in contrast to paths that do not encircle the EP3. The winding topology of the three energy bands is clearly revealed by the extracted complex eigenenergies with respect to θ , as shown in Fig. 1f through measuring the spectral lines along this path. This feature can also be characterized by the winding number relative to an energy E_B inside a loop⁵⁴

$$W = \int_0^{2m\pi} \frac{d\theta}{2m\pi} \partial_{\theta} \arg(E_n(\theta) - E_B), \quad (7)$$

where E_n is the complex eigenenergy of the n th band, and m is the smallest integer so that $E_n(\theta) = E_n(\theta + 2\pi m)$ (here $m = 3$) [we define $E_n(\theta + 2\pi k) = E_{(n+k) \bmod m}(\theta)$ so that $E_n(\theta)$ is continuous over θ]. Our results demonstrate that $W = 1/3$, indicating the 6π periodicity of each band (see “Methods” in Non-Hermitian absorption spectroscopy).

Eigenstate tomography

A definitive feature of an EP3 is the coalescence of three eigenstates into a single eigenstate at this point. We now demonstrate the coalescence through eigenstate tomography, where we scan the Hilbert space to identify the eigenstates of the non-Hermitian Hamiltonian H_{eff} without the requirement of an auxiliary level. Unfortunately, the dynamics described by Eq. (1) in the absence of an auxiliary level is not equivalent to the dynamics of a non-Hermitian Hamiltonian H_{eff} . We

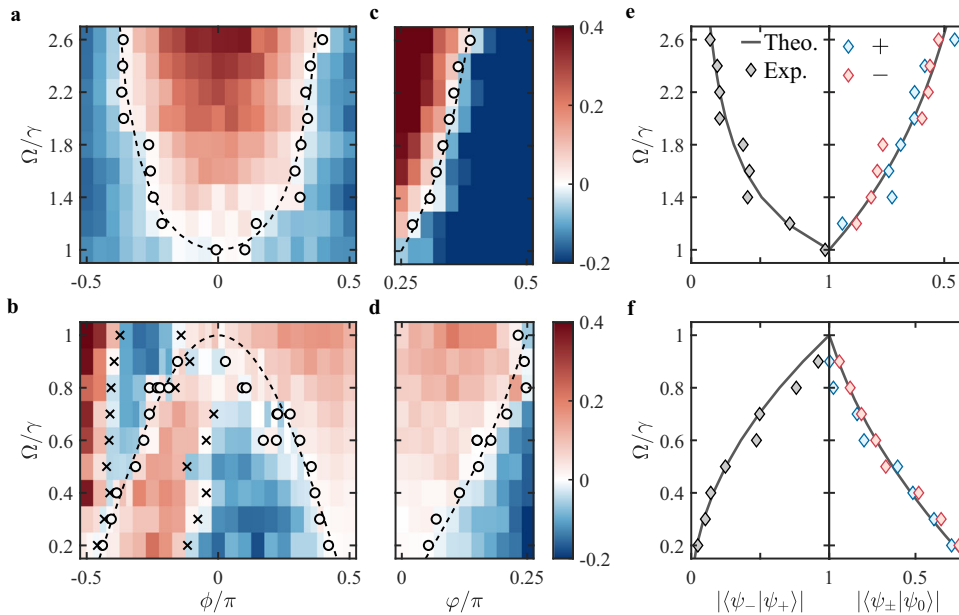


Fig. 2 | Experimental results for eigenstate tomography. a–d Variation of the normalized off-diagonal elements $\Delta|\rho_{i3}^n|^2$ with respect to ϕ (or φ) and Ω/γ . The initial state is $|u_z(\phi)\rangle$ in (a), $|u_x(\phi)\rangle$ in (b) and $|u_0(\varphi)\rangle$ in (c, d) (see their definitions in the main text). In (a, c, d), $j=2$, and in (b) $j=1$. The circles indicate the zero points obtained by linearly interpolating the experimental data (see “Methods” in Eigenstate tomography), and the black dashed lines represent the theoretical values:

$\phi = \pm \cos^{-1}(\gamma/\Omega)$ for (a) $\phi = \pm \cos^{-1}(\Omega/\gamma)$ for (b) and $\varphi = \tan^{-1}(\Omega/\gamma)$ for (c, d). The crosses in (b) also denote zero points but are excluded in the calculation of inner products since they do not correspond to the eigenstates. e, f Inner products of the eigenstates $|\psi_{\pm}\rangle$ and $|\psi_0\rangle$ for the PT symmetry-unbroken ($\Omega/\gamma > 1$) and broken regime ($\Omega/\gamma < 1$). The solid lines are obtained by Eq. (4), and the diamonds are experimental data.

address the problem by finding, based on Eq. (1), that an off-diagonal sector $v(t) = (\rho_{03}(t), \rho_{13}(t), \rho_{23}(t))^T$ of the density matrix $\rho(t)$ satisfies a non-Hermitian evolution: $d\rho_{n3}/dt = -i\langle n|H_{\text{eff}}\rho|3\rangle$ for $n = 0, 1, 2$ so that $v(t) = e^{-iH_{\text{eff}}t}v(0)$ (see “Methods” Quench dynamics for the derivation). Thus, the PT transition can be detected by initially preparing a pure state $\rho(0) = \frac{1}{2}(|\psi\rangle + |3\rangle)(\langle\psi| + \langle 3|)$ and monitoring the dynamics of $v(t)$ by measuring the off-diagonal sector $v(t)$ of the evolving density matrix (see Supplementary Information S-3 on how we measure the off-diagonal elements).

If $|\psi\rangle$ is an eigenstate of H_{eff} , then $v(t)$ will experience only an overall decay in amplitude, and the normalized off-diagonal elements $\rho_{i3}^n(t) = \rho_{i3}^n(0)/|v(t)|$ ($i = 0, 1, 2$) should remain invariant during the evolution. Therefore, the zero points of the variation of the normalized off-diagonal elements $\Delta|\rho_{i3}^n|^2 = |\rho_{i3}^n(\Delta t)|^2 - |\rho_{i3}^n(0)|^2$ with respect to $|\psi\rangle$ reveal the eigenstates of H_{eff} . The presence of PT and anti-PT symmetry significantly simplifies the procedure by imposing constraints that reduce the dimension of the search space. Based on these symmetries and additional constraints imposed by the Hamiltonian, we only need to scan a parameter space specified by $|u_z(\phi)\rangle = \frac{1}{2}(-e^{i\phi}, i\sqrt{2}, e^{-i\phi})^T$ for $\Omega > \gamma$, $|u_x(\phi)\rangle = (-\frac{1+\sin\phi}{2}, i\frac{\cos\phi}{\sqrt{2}}, \frac{1-\sin\phi}{2})^T$ for $\Omega < \gamma$, and $|u_0(\varphi)\rangle = \frac{1}{\sqrt{2}}(-\sin\varphi, i\sqrt{2}\cos\varphi, \sin\varphi)^T$ for all Ω (see Methods in Eigenstate tomography). $|u_z(\phi)\rangle$ and $|u_x(\phi)\rangle$ become the eigenstates $|\psi_{\pm}\rangle$ when $\phi = \pm \cos^{-1}(\gamma/\Omega)$ for $\Omega > \gamma$ and $\phi = \pm \cos^{-1}(\Omega/\gamma)$ for $\Omega < \gamma$, respectively, and $|u_0(\varphi)\rangle = |\psi_0\rangle$ when $\varphi = \tan^{-1}(\Omega/\gamma)$. Specifically, $|u_z(\phi)\rangle = |u_x(\phi)\rangle = |u_0(\varphi)\rangle = |\text{EP}\rangle$ when $\phi = 0$ and $\varphi = \pi/4$.

Figure 2 a shows the variation $\Delta|\rho_{23}^1|^2$ with respect to ϕ and Ω/γ for $\Omega > \gamma$ with the initial state being $|u_z(\phi)\rangle$, while Fig. 2b displays $\Delta|\rho_{13}^1|^2$ for $\Omega < \gamma$ with the initial state being $|u_x(\phi)\rangle$. Regions where $\Delta|\rho_{i3}^n|^2 \approx 0$ are highlighted in white. The zero points of $\Delta|\rho_{i3}^n|^2$ are determined by linear interpolation between adjacent experimental data points of opposite signs (see Methods in Eigenstate tomography). These zero points, indicated by circles, show good agreement with the theoretical values

(dashed lines). We extract the eigenstates as $|\psi_{\pm}\rangle = |u_z(\phi_{\pm})\rangle$ for $\Omega > \gamma$ and $|\psi_{\pm}\rangle = |u_x(\phi_{\pm})\rangle$ for $\Omega < \gamma$, where ϕ_{+} and ϕ_{-} are the average values of the zero points in $\phi > 0$ and $\phi < 0$ regions, respectively. In the $\phi < 0$ region of Fig. 2b, we exclude the smallest and largest zero points (marked by crosses), as they do not correspond to the eigenstates. Similarly, the eigenstate $|\psi_0\rangle$ is extracted by using $|u_0(\varphi)\rangle$ as the initial states (see Fig. 2c, d). The eigenstate is given by $|\psi_0\rangle = |u_0(\varphi_0)\rangle$ with φ_0 being the average value of the zero points, marked by circles in Fig. 2c, d. To illustrate the collapse of the three states to a single one at the EP3, we show the inner products $\langle \psi_{-} | \psi_{+} \rangle$ and $\langle \psi_{\pm} | \psi_0 \rangle$ of the measured states for the PT symmetry-unbroken and broken regime in Fig. 2e and f, respectively. The results demonstrate that as Ω/γ approaches 1, the three eigenstates become increasingly aligned and eventually coalesce into a single vector at $\Omega/\gamma=1$, experimentally confirming the existence of an EP3.

We further demonstrate the EP3 associated with the PT symmetry breaking through quench dynamics from an initial state $\rho(0) = (1/2)(|0\rangle + |3\rangle)(\langle 0| + \langle 3|)$. We find that the density matrix element ρ_{03} exhibits oscillatory and decaying behaviors for $\Omega > \gamma$ and $\Omega < \gamma$, respectively (see “Methods” in Quench dynamics), providing further evidence that all three eigenenergies transition from purely real to purely imaginary across the EP3.

Liouvillian EP3

EPs can also occur in the Liouvillian spectrum^{48,55–58}. In fact, the non-Hermitian EP3 discussed in previous sections can be regarded as a Liouvillian EP3. Specifically, for $\rho_n^R = |\psi_n\rangle\langle 3|$ with $n = 0, +, -$, we have $\mathcal{L}[\rho_n^R] = -iE_n\rho_n^R$. Thus, the three eigenmatrices coalesce into a single density matrix $|\text{EP}\rangle\langle 3|$ at $\Omega = \gamma$. Similarly, for $\rho_n^L = |3\rangle\langle\psi_n|$, we find $\mathcal{L}[\rho_n^L] = iE_n^*\rho_n^L$. This Liouvillian EP3 originates purely from the effective non-Hermitian Hamiltonian, as seen in the relation that $\mathcal{L}[\rho_n^R] = -iH_{\text{eff}}\rho_n^R$ and $\mathcal{L}[\rho_n^L] = i\rho_n^L H_{\text{eff}}^\dagger$ (see Methods in Liouvillian EP3 for more details). This raises the question of whether an intrinsic EP3 exists for the Liouvillian itself. Interestingly, we identify three eigenmatrices, ρ_{\pm} and ρ_0 , with

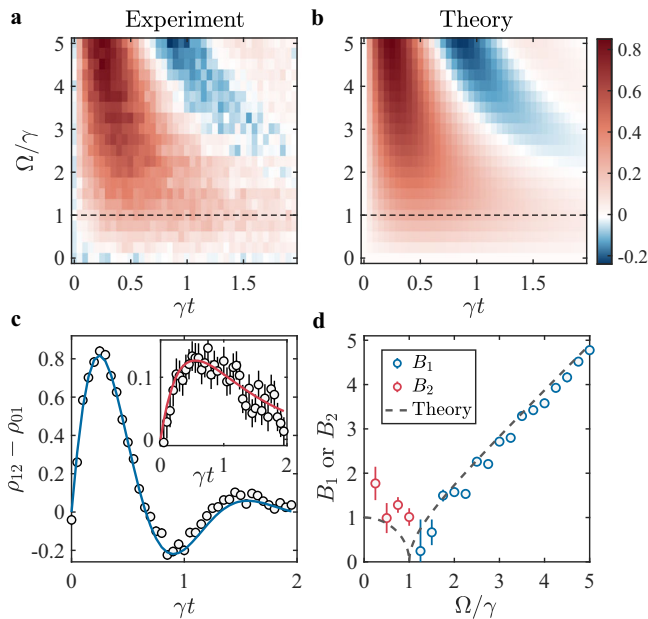


Fig. 3 | Results for observing a Liouvillian EP3 via quench dynamics. **a** Experimental and **(b)** theoretical values of $\rho_{12} - \rho_{01}$ with respect to the normalized evolution time γt and the ratio Ω/γ . The dashed lines indicate the evolution results at the EP3. **c** Curve fitting using the damped sinusoidal function for experimental data (circles) at $\Omega/\gamma = 5$. The inset shows the fitting results using the hyperbolic sine function at $\Omega/\gamma = 0.5$. The experimental data are averaged over 1000 repetitions. **d** Fitted oscillation and decay factors B_1 and B_2 with respect to Ω/γ . The theoretical results are $B_{1,2} = |\sqrt{(\Omega/\gamma)^2 - 1}|$ (see Method in Liouvillian EP3). Error bars, some of which are smaller than the symbols, denote the 95% confidence intervals of the fit.

eigenvalues $\lambda_{\pm} = -2\gamma \pm i\sqrt{\Omega^2 - \gamma^2}$ and $\lambda_0 = -2\gamma$ (see “Methods” in Liouvillian EP3E. 1), distinct from the aforementioned eigenmatrices as they do not involve $|3\rangle$. These eigenmatrices coalesce into a single density matrix $\rho_{EP} = |0\rangle\langle 1| + |1\rangle\langle 2| + i\sqrt{2}|0\rangle\langle 2| + \text{H.c.}$ at $\Omega = \gamma$, with the eigenvalues transitioning between purely real and purely imaginary up to a constant shift.

To detect the Liouvillian EP3 associated with the PT transition, we use a non-physical initial state $\rho(0) = |u_1\rangle\langle u_1| - |u_2\rangle\langle u_2|$, where $|u_n\rangle = \frac{1}{\sqrt{2}}(|0\rangle + i(-1)^n|2\rangle)$ for $n = 1, 2$. Due to the anti-PT symmetry of the open quantum system, elements of $\rho(t)$ can be detected by preparing a single state $\sigma(0) = |u_1\rangle\langle u_1|$ and measuring the elements of $\sigma(t)$ (see Methods Detection of the intrinsic Liouvillian EP3). The experimentally measured off-diagonal elements $\rho_{12} - \rho_{01}$, shown in Fig. 3a, along with the theoretical results in Fig. 3b, reveal that $\rho_{12} - \rho_{01}$ oscillates when $\Omega > \gamma$ and decays exponentially after the first peak when $\Omega < \gamma$, indicating the PT symmetry breaking at $\Omega = \gamma$. We further fit $\rho_{12} - \rho_{01}$ to damped sinusoidal and hyperbolic sine functions given by $f_1(\gamma t) = A_1 e^{-2\gamma t} \sin(B_1 \gamma t)$ and $f_2(\gamma t) = A_2 e^{-2\gamma t} \sinh(B_2 \gamma t)$, respectively, as shown in Fig. 3c. We find that in the PT symmetry unbroken (symmetry-broken) phase, the former (latter) fitting function yields a lower error than the latter (former) with the corresponding fitted oscillation factor B_1 and decay factor B_2 shown in Fig. 3d. The results clearly indicate the PT transition of the Lindbladian \mathcal{L} at $\Omega = \gamma$.

In summary, we have experimentally detected an EP3 associated with PT symmetry breaking in a dissipative trapped ion system, focusing on both the non-Hermitian and Liouvillian aspects. For the non-Hermitian case, we demonstrate the existence of an EP3 and the PT transition via non-Hermitian absorption spectroscopy, eigenstate tomography, and quench dynamics. For the Liouvillian case, we show that the non-Hermitian EP3s can also be interpreted as Liouvillian EP3s. We further experimentally identify an intrinsic Liouvillian EP3 associated

with a PT transition by quench dynamics. These results may enable further exploration of peculiar non-Hermitian topological properties, such as braiding of three complex energy bands^{59,60}, and non-Hermitian applications, such as chiral state transfer⁴⁸ and sensing, in a dissipative quantum system. EPs of orders higher than three can also be achieved by introducing additional energy levels and engineered losses. In addition, given that the EP3 is implemented through precise control of dissipation, this technology has the potential to advance quantum computation, quantum simulation and quantum metrology^{61,62}.

Note added in proof. After the submission of this manuscript, we became aware of a related study reporting the experimental realization of a fourth-order exceptional point in a trapped $^{40}\text{Ca}^+$ ion⁶³.

Methods

Adiabatic elimination for the master equation

The dynamics of the full system described in Fig. 1b is governed by the Lindblad master equation ($\hbar = 1$)

$$\frac{d\rho_f}{dt} = -i[H_f, \rho_f] + \sum_{\mu=1}^6 (L_{f,\mu} \rho_f L_{f,\mu}^\dagger - \frac{1}{2} \{L_{f,\mu}^\dagger L_{f,\mu}, \rho_f\}), \quad (8)$$

where $H_f = H + (J_1|1\rangle\langle e_1| + J_2|2\rangle\langle e_2| + \text{H.c.})$ with $H = \frac{\Omega}{\sqrt{2}}|0\rangle\langle 1| + \frac{\Omega}{\sqrt{2}}|1\rangle\langle 2| + \text{H.c.}$, $L_{f,1} = c|0\rangle\langle e_1|$, $L_{f,2} = c|1\rangle\langle e_1|$, $L_{f,3} = c|3\rangle\langle e_1|$, $L_{f,4} = c|0\rangle\langle e_2|$, $L_{f,5} = c|2\rangle\langle e_2|$, $L_{f,6} = c|3\rangle\langle e_2|$, and $c = \sqrt{\Gamma/3}$. Here, $\Omega_{1,2}$ ($J_{1,2}$) are controlled by the microwaves (370 nm lasers B and C), and $\Gamma = 1/\tau_p \approx 2\pi \times 19.6$ MHz with $\tau_p \approx 8.12$ ns being the lifetime of the $^2P_{1/2}$ states⁶⁴. Note that theoretically we have neglected the decay of the $^2P_{1/2}$ states towards $^2D_{3/2}$ due to the small branching ratio (-0.5%), and experimentally we use a 935 nm laser to pump the leakage into $^2D_{3/2}$ back to the $^2S_{1/2}$ manifold (see Supplementary Information S-1 for details). The full system master equation [Eq. (8)] can be rewritten as

$$\begin{aligned} \frac{d\rho_f}{dt} = & -i[H_f, \rho_f] + \frac{\Gamma}{3} \rho_{e_1 e_1} (|0\rangle\langle 0| + |1\rangle\langle 1| + |3\rangle\langle 3|) \\ & + \frac{\Gamma}{3} \rho_{e_2 e_2} (|0\rangle\langle 0| + |2\rangle\langle 2| + |3\rangle\langle 3|) \\ & - \frac{\Gamma}{2} \{|e_1\rangle\langle e_1|, \rho\} - \frac{\Gamma}{2} \{|e_2\rangle\langle e_2|, \rho\}. \end{aligned} \quad (9)$$

Let $P = |0\rangle\langle 0| + |1\rangle\langle 1| + |2\rangle\langle 2| + |3\rangle\langle 3|$ be the projection operator onto the $^2S_{1/2}$ ground state manifold. Applying P to the master equation [Eq. (9)], we obtain

$$\begin{aligned} \frac{d\rho}{dt} = & (-iH\rho - iJ_1|1\rangle\langle e_1|\rho_f P - iJ_2|2\rangle\langle e_2|\rho_f P + \text{H.c.}) \\ & + \frac{\Gamma}{3} \rho_{e_1 e_1} (|0\rangle\langle 0| + |1\rangle\langle 1| + |3\rangle\langle 3|) \\ & + \frac{\Gamma}{3} \rho_{e_2 e_2} (|0\rangle\langle 0| + |2\rangle\langle 2| + |3\rangle\langle 3|), \end{aligned} \quad (10)$$

where $\rho = P\rho_f P$. Notice that Eq. (10) involves $\rho_{e_1\mu}$ and $\rho_{e_2\mu}$ ($\mu = 0, 1, 2, 3$), as well as $\rho_{e_1 e_1}$ and $\rho_{e_2 e_2}$. We can derive an equation involving only the $^2S_{1/2}$ levels using adiabatic elimination. From Eq. (9), we have

$$\begin{aligned} \frac{d\rho_{e_1 0}}{dt} &= -iJ_1\rho_{10} + i\frac{\Omega_1}{\sqrt{2}}\rho_{e_1 1} - \frac{\Gamma}{2}\rho_{e_1 0}, \\ \frac{d\rho_{e_1 1}}{dt} &= -iJ_1\rho_{11} + i\frac{\Omega_1}{\sqrt{2}}\rho_{e_1 0} + i\frac{\Omega_2}{\sqrt{2}}\rho_{e_1 2} + iJ_1\rho_{e_1 e_1} - \frac{\Gamma}{2}\rho_{e_1 1}, \\ \frac{d\rho_{e_1 2}}{dt} &= -iJ_1\rho_{12} + i\frac{\Omega_2}{\sqrt{2}}\rho_{e_1 1} + iJ_2\rho_{e_1 e_2} - \frac{\Gamma}{2}\rho_{e_1 2}, \\ \frac{d\rho_{e_1 3}}{dt} &= -iJ_1\rho_{13} - \frac{\Gamma}{2}\rho_{e_1 3}, \\ \frac{d\rho_{e_1 e_1}}{dt} &= -iJ_1\rho_{1e_1} + iJ_1\rho_{e_1 1} - \Gamma\rho_{e_1 e_1}. \end{aligned} \quad (11)$$

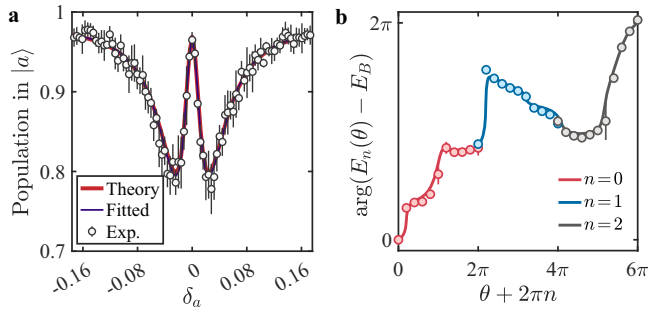


Fig. 4 | Spectral line and winding topology. **a** The spectral line (the remaining population in $|a\rangle$) at the end of the dynamics at $t_a = 200 \mu\text{s}$ with respect to the detuning δ_a for $\Omega/\gamma = 0.8$. Here, the half-width of the outer dips is mainly determined by $\text{Im}(E_0 - iy)$, while the half-width of the inner peak is mainly determined by $\text{Im}(E_+ - iy)$. Both the theoretical results (red line) and fitted ones (black line) are calculated according to Eq. (21). The former ones are computed using the parameter $\Omega/\gamma = 0.8$, while the fitted results employ parameters obtained from a fitting procedure based on the experimental data (circles). **b** Argument of $E_n(\theta) - E_B$ as a function of θ with $E_B = -0.016 - 0.032i$ plotted using the data in Fig. 1f. The y-axis is shifted so that $\arg(E_0(0) - E_B) = 0$, and the n -th band is shifted along the x-axis by $2\pi n$ to show the spectral winding around E_B . The units of energy is $2\pi \times 1 \text{ MHz}$. Here, $\gamma = 2\pi \times 0.040 \text{ MHz}$ and $\Omega_a = 2\pi \times 0.004 \text{ MHz}$. The experimental results are averaged over 5 rounds of experiments (each contains 200 shots) with error bars being the standard deviation of the 5 experimental repetitions.

We assume $J_1, J_2 \ll \Gamma$ so that the population in $|e_1\rangle$ is small, giving rise to $d\rho_{e_1\nu}/dt \approx 0$ for any ν . We also have $\rho_{e_1\nu} \ll \rho_{ij}$ for $i, j = 0, 1, 2, 3$, allowing us to omit the $\rho_{e_1\nu}$ terms in Eq. (11) that are not multiplied by Γ . This gives

$$\begin{aligned} \rho_{e_1\mu} &\approx -i \frac{2J_1}{\Gamma} \rho_{1\mu}, \\ \rho_{e_1e_1} &\approx \frac{4J_1^2}{\Gamma^2} \rho_{11}, \end{aligned} \quad (12)$$

for $\mu = 0, 1, 2, 3$. Similarly, for $|e_2\rangle$, we obtain

$$\begin{aligned} \rho_{e_2\mu} &\approx -i \frac{2J_2}{\Gamma} \rho_{2\mu}, \\ \rho_{e_2e_2} &\approx \frac{4J_2^2}{\Gamma^2} \rho_{22}. \end{aligned} \quad (13)$$

Using Eq. (12) and Eq. (13), we have $\langle e_1 | \rho_f P = -i(2J_1/\Gamma) \langle 1 | \rho$ and $\langle e_2 | \rho_f P = -i(2J_2/\Gamma) \langle 2 | \rho$. Eq. (10) becomes

$$\begin{aligned} \frac{d\rho}{dt} &= (-iH\rho - \gamma_1|1\rangle\langle 1|\rho - \gamma_2|2\rangle\langle 2|\rho + \text{H.c.}) \\ &+ \frac{2\gamma_1}{3} \rho_{11}(|0\rangle\langle 0| + |1\rangle\langle 1| + |3\rangle\langle 3|) \\ &+ \frac{2\gamma_2}{3} \rho_{22}(|0\rangle\langle 0| + |2\rangle\langle 2| + |3\rangle\langle 3|), \end{aligned} \quad (14)$$

which is the same as Eq. (1) with $\gamma_1 = 2J_1^2/\Gamma$ and $\gamma_2 = 2J_2^2/\Gamma$. We have numerically confirmed that the results from Eq. (1) agree well with those from the full dynamics [Eq. (8)] given that $J_1, J_2 \ll \Gamma$.

Non-Hermitian absorption spectroscopy

By weakly coupling a system level with an auxiliary energy level $|a\rangle$ and using $|a\rangle$ as the initial state, we can eliminate the effects of quantum jumps. The Hamiltonian H (similarly for H_f) becomes $H' = H + \frac{\Omega_a}{2}(|1\rangle\langle a| + \text{H.c.}) - \delta_a|a\rangle\langle a|$. By a similar adiabatic elimination of $|e_1\rangle$ and $|e_2\rangle$ levels, one also arrives at Eq. (14) with $H \rightarrow H'$. We project Eq. (14) onto the subspace spanned by the system and auxiliary

levels using $P_a = |0\rangle\langle 0| + |1\rangle\langle 1| + |2\rangle\langle 2| + |a\rangle\langle a|$. Then we have

$$\frac{d\rho_a}{dt} = (-iH_{\text{NAS}}\rho_a + \text{H.c.}) + \sum_{n=1}^2 \frac{2\gamma_n}{3} \rho_{nn}(|0\rangle\langle 0| + |n\rangle\langle n|), \quad (15)$$

with $\rho_a = P_a \rho P_a$ and H_{NAS} given by Eq. (5). The dynamics of ρ_{11} and ρ_{22} are given by

$$\begin{aligned} \frac{d\rho_{11}}{dt} &= -\frac{4\gamma_1}{3} \rho_{11} - \left(i \frac{\Omega_1}{\sqrt{2}} \rho_{01} + i \frac{\Omega_2}{\sqrt{2}} \rho_{21} + i \frac{\Omega_a}{2} \rho_{a1} + \text{H.c.} \right), \\ \frac{d\rho_{22}}{dt} &= -\frac{4\gamma_2}{3} \rho_{22} - \left(i \frac{\Omega_2}{\sqrt{2}} \rho_{12} + \text{H.c.} \right). \end{aligned} \quad (16)$$

Given that Ω_a is sufficiently small, we have $\rho_{11} \approx 0$ and $\rho_{22} \approx 0$ due to the dissipation terms $-\frac{4\gamma_1}{3} \rho_{11}$ and $-\frac{4\gamma_2}{3} \rho_{22}$ in Eq. (16). As a result, the second term on the right-hand side of Eq. (15) can be omitted, and the state satisfies a non-Hermitian evolution by H_{NAS} .

We now derive the population in $|a\rangle$ by incorporating the fact that this state has a finite lifetime. Ideally, the population in $|a\rangle$ satisfies a non-Hermitian evolution given by

$$N_a^{\text{NH}}(t) = |\langle a | e^{-iH_{\text{NAS}}t} | a \rangle|^2 = e^{-\kappa t}, \quad (17)$$

where κ is the transfer rate from $|a\rangle$ to the system levels. In practice, the $D_{S/2}$ state $|a\rangle$ has a finite lifetime of $\tau_a \approx 7.4 \text{ ms}$. Considering the finite lifetime of $|a\rangle$ and the state detection and measurement errors, the actual population in $|a\rangle$ is approximately described by

$$N_a(t) = N_0 e^{-(\gamma_a + \kappa)t} = N_0 e^{-\gamma_a t} N_a^{\text{NH}}(t), \quad (18)$$

with $\gamma_a = 1/\tau_a$.

In our experiment, the measured population in $|a\rangle$ is 1 subtracted by the population in the ${}^2S_{1/2}$ manifold, given by

$$N_a^{\text{tgt}}(t) = 1 - N_s(t) = N_a(t) + N_f(t), \quad (19)$$

where N_f is the population in the ${}^2F_{7/2}$ state. The branching ratio of $D_{S/2} \rightarrow {}^2F_{7/2}$ is 81.6%⁶⁴, thus N_f satisfies $dN_f/dt = 0.816\gamma_a N_a$. Solving the differential equation with the initial condition $N_f(0) = 0$, we obtain

$$\begin{aligned} N_f(t) &= \frac{0.816\gamma_a}{\gamma_a + \kappa} N_0 [1 - e^{-(\gamma_a + \kappa)t}] \\ &= \frac{0.816\gamma_a}{\gamma_a - \frac{1}{\tau} \ln[N_a^{\text{NH}}(t)]} N_0 [1 - e^{-\gamma_a t} N_a^{\text{NH}}(t)]. \end{aligned} \quad (20)$$

Finally, we obtain the theoretical value of the experimentally measured population in $|a\rangle$ given by

$$\begin{aligned} N_a^{\text{tgt}}(t) &= N_0 e^{-\gamma_a t} N_a^{\text{NH}}(t) \\ &+ \frac{0.816\gamma_a}{\gamma_a - \frac{1}{\tau} \ln[N_a^{\text{NH}}(t)]} N_0 [1 - e^{-\gamma_a t} N_a^{\text{NH}}(t)], \end{aligned} \quad (21)$$

which is used in non-Hermitian absorption spectroscopy.

The system parameters are extracted by minimizing the loss function $L = \sum L_i$, with

$$L_i = \sum_{\delta_a} \left[N_{a,i}^{\text{exp}}(\delta_a) - N_{a,i}^{\text{tgt}}(\delta_a; \mathbf{P}_i) \right]^2. \quad (22)$$

Here $N_{a,i}^{\text{exp}}(\delta_a)$ is the experimentally measured population in the auxiliary level at detuning δ_a (e.g., Fig. 4a), and $N_{a,i}^{\text{tgt}}(\delta_a; \mathbf{P}_i)$ denotes the theoretically calculated population based on the system parameters \mathbf{P}_i . The theoretical population $N_{a,i}^{\text{tgt}}$ is calculated from Eq. (21). The system parameters are given by $\mathbf{P}_i = \{\Omega_{1,i}, \Omega_{2,i}, \gamma_{1,i}, \gamma_{2,i}, N_{0,i}\}$ (or with additional detuning terms $\{\Delta_{0,i}, \Delta_{1,i}\}$), where i is the index for the ratio Ω/γ . We

impose constraints on the fitting parameters based on the experimental setup. Specifically, we assume $\Omega_{1,i} = \Omega_{2,i}$ since the microwave amplitudes can be controlled with high precision. For the decay rates $\gamma_{1,i}$ and $\gamma_{2,i}$, due to the drift in the laser power, we cannot simply assume $\gamma_{2,i} = 2\gamma_{1,i}$. However, we manage to control the laser power (proportional to $J_{1,2}^2$) within a 5% deviation from the initial value. Thus, we assume that $\bar{\gamma}_2 = 2\bar{\gamma}_1$, where $\bar{\gamma}_n$ denotes the average of $\gamma_{n,i}$ over all i , and each $\gamma_{n,i}$ is constrained to be within a 5% deviation from $\bar{\gamma}_n$. Once the system parameters are obtained through fitting, we calculate the eigenenergies of the non-Hermitian Hamiltonian.

In Fig. 1f, we show the extracted complex eigenenergies as a function of θ . Here, we further provide $\arg(E_n(\theta) - E_B)$ in Fig. 4b, clearly illustrating the 6π periodicity of each band.

In addition, we note that adding the auxiliary level $|a\rangle$ and its coupling with the system levels inevitably lifts the EP3 degeneracy in the total Hamiltonian H_{NAS} . The effect vanishes in the ideal case where the coupling $\Omega_a \rightarrow 0$, the evolution time $t_a \rightarrow \infty$, and $\Omega_a^2 t_a$ remains a constant. However, due to experimental imperfections, the evolution time t_a is limited by the coherence time and other errors. Consequently, a finite Ω_a is required to obtain a finite signal. Although the finite coupling slightly perturbs the degeneracy, experimental errors make this perturbation negligible.

Quench dynamics

To eliminate the effects of quantum jumps, one can also utilize an off-diagonal sector in the density matrix, which follows a pure non-Hermitian evolution. We show this by writing down the density matrix in a block form,

$$\rho = \begin{pmatrix} \rho_{\text{sys}} & v \\ w & \rho_{33} \end{pmatrix}, \quad (23)$$

with

$$\rho_{\text{sys}} = \begin{pmatrix} \rho_{00} & \rho_{01} & \rho_{02} \\ \rho_{10} & \rho_{11} & \rho_{12} \\ \rho_{20} & \rho_{21} & \rho_{22} \end{pmatrix}, v = \begin{pmatrix} \rho_{03} \\ \rho_{13} \\ \rho_{23} \end{pmatrix}, w = \begin{pmatrix} \rho_{30} \\ \rho_{31} \\ \rho_{32} \end{pmatrix}^T. \quad (24)$$

The master equation in Eq. (1) can be written as

$$\frac{d}{dt} \begin{pmatrix} \rho_{\text{sys}} & v \\ w & \rho_{33} \end{pmatrix} = -i \begin{pmatrix} H_{\text{eff}} & \mathbf{0} \\ \mathbf{0} & 0 \end{pmatrix} \begin{pmatrix} \rho_{\text{sys}} & v \\ w & \rho_{33} \end{pmatrix} + i \begin{pmatrix} \rho_{\text{sys}} & v \\ w & \rho_{33} \end{pmatrix} \begin{pmatrix} H_{\text{eff}}^\dagger & \mathbf{0} \\ \mathbf{0} & 0 \end{pmatrix} + \mathcal{D}[\rho], \quad (25)$$

where H_{eff} is the 3×3 non-Hermitian matrix in Eq. (2) and

$$\mathcal{D}[\rho] = \sum_{\mu} L_{\mu} \rho L_{\mu}^\dagger = \begin{pmatrix} c_1 \rho_{11} + c_2 \rho_{22} & 0 & 0 & 0 \\ 0 & c_1 \rho_{11} & 0 & 0 \\ 0 & 0 & c_2 \rho_{22} & 0 \\ 0 & 0 & 0 & c_1 \rho_{11} + c_2 \rho_{22} \end{pmatrix}. \quad (26)$$

Based on this equation, we find that

$$\frac{dv}{dt} = -i H_{\text{eff}} v, \quad (27)$$

giving rise to

$$v(t) = e^{-i H_{\text{eff}} t} v(0). \quad (28)$$

More generally, if the Hilbert space splits into two orthogonal subspaces S and S' such that the Hamiltonian acts trivially on $|s'\rangle \in S'$, i.e.,

$$H = \begin{pmatrix} H_{SS} & \mathbf{0} \\ \mathbf{0} & \mathbf{0} \end{pmatrix}, \quad (29)$$

and each jump operator has one of the block forms

$$L_{\mu} = \begin{pmatrix} L_{\mu,SS} & \mathbf{0} \\ \mathbf{0} & \mathbf{0} \end{pmatrix} \quad \text{or} \quad L_{\mu} = \begin{pmatrix} \mathbf{0} & \mathbf{0} \\ L_{\mu,S'S} & \mathbf{0} \end{pmatrix}, \quad (30)$$

where the first and second row/column correspond to S and S' , respectively, then

1. The effective Hamiltonian $H_{\text{eff}} = H - \frac{i}{2} \sum_{\mu} L_{\mu}^\dagger L_{\mu}$ also acts trivially on $|s'\rangle \in S'$,
2. The off-diagonal sector $\rho_{SS'}$ of the density matrix follows a non-Hermitian evolution $d\rho_{SS'}/dt = -i H_{\text{eff}} \rho_{SS'}$ with $\rho_{SS'}$ being a submatrix in the density matrix

$$\rho = \begin{pmatrix} \rho_{SS} & \rho_{SS'} \\ \rho_{S'S} & \rho_{S'S'} \end{pmatrix}. \quad (31)$$

In our case, $S = \text{span}\{|0\rangle, |1\rangle, |2\rangle\}$ and $S' = \text{span}\{|3\rangle\}$. We note that this condition can always be realized by introducing an additional level that does not couple to any other levels via the Hamiltonian and the jump operators.

In the following, we show a specific application of the aforementioned technique on studying the PT-symmetry breaking in our system (such dynamics can also be used to study other non-Hermitian applications, such as state transfer⁴⁸). We consider an initial state $\rho(0) = \frac{1}{2}(|0\rangle + |3\rangle)(\langle 0| + \langle 3|)$, so that $v(0) = \frac{1}{2}(1, 0, 0)^T = \frac{\Omega}{4(\Omega^2 - \gamma^2)}[(\gamma - i\sqrt{\Omega^2 - \gamma^2})|\psi_+\rangle + (\gamma + i\sqrt{\Omega^2 - \gamma^2})|\psi_-\rangle - \sqrt{2(\Omega^2 + \gamma^2)}|\psi_0\rangle]$. Since the off-diagonal element ρ_{03} evolves as $v(t) = e^{-i H_{\text{eff}} t} v(0)$, we have $\rho_{03}(t) = [v(t)]_0 = \frac{\Omega^2 e^{-\gamma t}}{4(\Omega^2 - \gamma^2)} [1 + \frac{\Omega^2 - 2\gamma^2}{\Omega^2} \cos(\sqrt{\Omega^2 - \gamma^2} t) + \frac{2\gamma\sqrt{\Omega^2 - \gamma^2}}{\Omega^2} \sin(\sqrt{\Omega^2 - \gamma^2} t)]$. Further simplification gives

$$\rho_{03}(t) = \frac{\Omega^2 e^{-\gamma t}}{2(\Omega^2 - \gamma^2)} \sin^2 \left(\frac{\sqrt{\Omega^2 - \gamma^2}}{2} t + C_1 \right), \quad (32)$$

with $C_1 = \cos^{-1}(\gamma/\Omega)$. For $\Omega < \gamma$, the equation becomes

$$\rho_{03}(t) = \frac{\Omega^2 e^{-\gamma t}}{2(\gamma^2 - \Omega^2)} \sinh^2 \left(\frac{\sqrt{\gamma^2 - \Omega^2}}{2} t + C_2 \right), \quad (33)$$

with $C_2 = \cosh^{-1}(\gamma/\Omega)$.

The experimentally measured off-diagonal element $|\rho_{03}|$, shown in Fig. 5a, agrees well with the theoretical results (Fig. 5b), providing a clear signature of the PT symmetry breaking across $\Omega = \gamma$. Specifically, for $\Omega > \gamma$, all eigenenergies are real (up to a constant shift), causing $|\rho_{03}|$ to oscillate with a frequency determined by the real eigenenergy. In contrast, for $\Omega < \gamma$, the eigenenergies become purely imaginary, leading $|\rho_{03}|$ to experience a pure decay. Based on Eq. (32) and Eq. (33), the time evolution of $|\rho_{03}|$ follows a damped sinusoidal (for $\Omega > \gamma$) or hyperbolic sine (for $\Omega < \gamma$) behavior, described by $f_1(\gamma t) = A_1 e^{-\gamma t} \sin^2(B_1 \gamma t + C_1)$ and $f_2(\gamma t) = A_2 e^{-\gamma t} \sinh^2(B_2 \gamma t + C_2)$, with

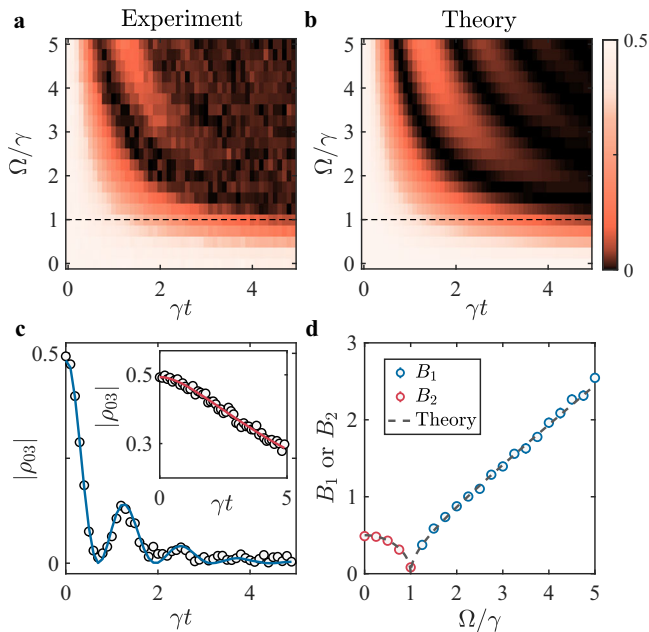


Fig. 5 | Results for quench dynamics. **a** Experimental and **(b)** theoretical results of an element $|\rho_{03}|$ of the density matrix with respect to the normalized evolution time γt and the ratio Ω/γ . **c** Curve fitting using the damped sinusoidal function for experimental data (circles) at $\Omega/\gamma = 5$. The inset shows the fitting results using the hyperbolic sine function at $\Omega/\gamma = 0.5$. The experimental data are averaged over 400 repetitions with error bars representing the standard deviation. **d** Fitted oscillation and decay factors B_1 or B_2 with respect to Ω/γ . The error bar, which is smaller than the symbols, denotes the 95% confidence intervals of the fit.

$B_1 = B_2 = \frac{1}{2} |\sqrt{(\Omega/\gamma)^2 - 1}|$. We fit the experimental data to both functions and select the one with the smallest error. Figure 5c displays the fitting result for $\Omega/\gamma = 5$, where $f_1(\gamma t)$ fits the experimental data best, while the inset for $\Omega/\gamma = 0.5$ is better characterized by $f_2(\gamma t)$. We find that in the symmetry unbroken region, the damped sinusoidal provides a better fitting than the hyperbolic sine function. Conversely, in the symmetry broken region, the hyperbolic sine function offers a better fit, consistent with theoretical results. In addition, we plot the fitted values of B_1 or B_2 with respect to Ω/γ in Fig. 5d, showing excellent agreement with theoretical results. The results clearly demonstrate a PT phase transition at $\Omega = \gamma$.

Eigenstate tomography

We assume that the eigenstate of the Hamiltonian is expressed as

$$|u_n\rangle = \begin{pmatrix} a_n + ib_n \\ c_n + id_n \\ e_n + if_n \end{pmatrix} \quad (34)$$

for $n = 0, +, -$. Due to the presence of PT and anti-PT symmetry, one of the eigenstate $|u_0\rangle$ must be symmetric under both PT and anti-PT operations, that is, $U_{PT}|u_0\rangle = e^{i\alpha}|u_0\rangle$ and $U_{APT}|u_0\rangle = e^{i\beta}|u_0\rangle$. By choosing an appropriate gauge, we can have $U_{PT}|u_0\rangle = e^{i\alpha}|u_0\rangle$ and $U_{APT}|u_0\rangle = |u_0\rangle$, resulting in $|u_0\rangle = (-e_0, id_0, e_0)^T$ or $\frac{1}{\sqrt{2}}(1, 0, 1)^T$. We exclude the latter case, as it is unlikely to be the eigenstate of an arbitrary Hamiltonian with PT and anti-PT symmetry. Let $e_0 = \frac{1}{\sqrt{2}} \sin \varphi$ and $d_0 = \cos \varphi$, we arrive at a normalized state

$$|u_0(\varphi)\rangle = \frac{1}{\sqrt{2}}(-\sin \varphi, i\sqrt{2} \cos \varphi, \sin \varphi)^T, \quad (35)$$

which becomes the eigenstate of H_{eff} when $\varphi = \tan^{-1}(\Omega/\gamma)$.

The other two states $|u_+\rangle$ and $|u_-\rangle$ are either PT or anti-PT symmetric. If they are PT symmetric (when $\Omega > \gamma$), we have $U_{PT}|u_+\rangle = -|u_+\rangle$, $U_{PT}|u_-\rangle = -|u_-\rangle$, and $U_{APT}|u_+\rangle = e^{i\alpha}|u_-\rangle$, where we have chosen a specific gauge for $|u_+\rangle$ and $|u_-\rangle$. These equations give rise to

$$|u_{\pm}\rangle = \frac{1}{\sqrt{2}} \begin{pmatrix} -re^{\pm i\phi} \\ i\sqrt{2(1-r^2)} \\ re^{\pm i\phi} \end{pmatrix}^T, \quad (36)$$

where r and ϕ are real numbers. In principle, one could scan the parameter space with respect to r and ϕ to identify the eigenstates. In our experiment, to reduce the amount of data required, we introduce another constraint based on the structure of the Hamiltonian. If $|u_+\rangle$ is an eigenstate of H_{eff} , then we have $(H_{\text{eff}} + i\gamma)|u_+\rangle = k|u_+\rangle$ with k being a real number, giving rise to $r = 1/\sqrt{2}$. As a result, we only need to prepare

$$|u_z(\phi)\rangle = \frac{1}{2} \begin{pmatrix} -e^{i\phi} \\ i\sqrt{2} \\ e^{-i\phi} \end{pmatrix}^T \quad (37)$$

for different values of ϕ to perform eigenstate tomography (see Supplementary Information S-2 for initial state preparation). $|u_z(\phi)\rangle$ becomes an eigenstate of H_{eff} when $\phi = \pm \cos^{-1}(\gamma/\Omega)$.

Similarly, if $|u_+\rangle$ and $|u_-\rangle$ are anti-PT symmetric (when $\Omega < \gamma$), then we have $U_{APT}|u_+\rangle = |u_+\rangle$, $U_{APT}|u_-\rangle = |u_-\rangle$, and $U_{PT}|u_+\rangle = e^{i\alpha}|u_-\rangle$, leading to

$$\begin{aligned} |u_+\rangle &= \begin{pmatrix} a, i\sqrt{1-(a^2+b^2)}, b \end{pmatrix}^T, \\ |u_-\rangle &= \begin{pmatrix} -b, i\sqrt{1-(a^2+b^2)}, a \end{pmatrix}^T, \end{aligned} \quad (38)$$

with a and b being real numbers. We also use $(H_{\text{eff}} + i\gamma)|u_+\rangle = ik|u_+\rangle$ and obtain another constraint $a - b = \pm 1$. Therefore, we can prepare the state

$$|u_x(\phi)\rangle = \begin{pmatrix} -\frac{1+\sin \phi}{2}, i\frac{\cos \phi}{\sqrt{2}}, \frac{1-\sin \phi}{2} \end{pmatrix}^T \quad (39)$$

for different ϕ , which becomes an eigenstate of H_{eff} when $\phi = \pm \cos^{-1}(\Omega/\gamma)$.

We note that these states can also be obtained by rotating the state $|EP\rangle$ around the z -axis (for $\Omega > \gamma$) or the x -axis (for $\Omega < \gamma$):

$$\begin{aligned} |u_z(\phi)\rangle &= e^{i\phi S_z} |EP\rangle, \\ |u_x(\phi)\rangle &= e^{i\phi S_x} |EP\rangle, \end{aligned} \quad (40)$$

with

$$S_z = \begin{pmatrix} 1 & 0 & 0 \\ 0 & 0 & 0 \\ 0 & 0 & -1 \end{pmatrix}, S_x = \frac{1}{\sqrt{2}} \begin{pmatrix} 0 & 1 & 0 \\ 1 & 0 & 1 \\ 0 & 1 & 0 \end{pmatrix} \quad (41)$$

being the spin-1 operators.

For eigenstate tomography in experiments, we determine the zero points of $\Delta|\rho_{13}^n|^2$ by linear interpolation between adjacent experimental data points of opposite signs, as shown in Fig. 6.

Liouvillian EP3

The Liouvillian superoperator can also be viewed as a non-Hermitian matrix in the doubled Hilbert space. By vectorizing the density matrix

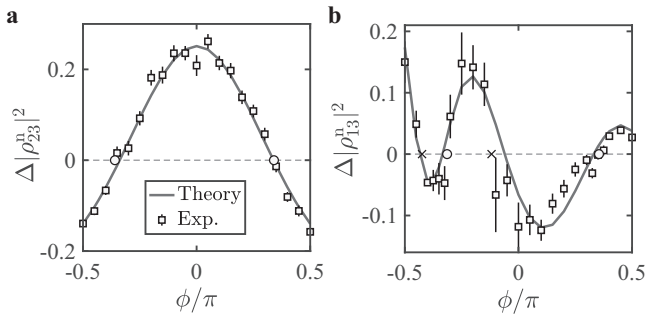


Fig. 6 | Determination of eigenstates in tomography. **a** $\Delta|\rho_{23}^n|^2$ as a function of ϕ with the initial state $|u_z(\phi)\rangle$ at $\Omega/\gamma=2$. **b** $\Delta|\rho_{23}^n|^2$ as a function of ϕ with the initial state $|u_x(\phi)\rangle$ at $\Omega/\gamma=0.5$. The zero points are marked by circles and crosses, determined by linear interpolation between adjacent experimental data points with opposite signs, and error bars denote the standard deviation.

through Choi-Jamiolkowski isomorphism^{65,66},

$$\rho = \sum_{ij} \rho_{ij} |i\rangle\langle j| \rightarrow |\rho\rangle = \sum_{ij} \rho_{ij} |i\rangle \otimes |j\rangle, \quad (42)$$

the master equation can be written as $d|\rho\rangle/dt = \mathcal{L}|\rho\rangle$ with

$$\mathcal{L} = -i(H_{\text{eff}} \otimes I - I \otimes H_{\text{eff}}^*) + \sum_{\mu} L_{\mu} \otimes L_{\mu}^*. \quad (43)$$

In this case, the Lindbladian of our model becomes a 16×16 non-Hermitian matrix which can also support EP3. Notably, certain Lindbladian eigenvectors are closely related to the Hamiltonian eigenstates. Given that $|\psi_n\rangle$ is the eigenstate of H_{eff} with eigenenergy E_n ($n=0, \pm$), $|\rho_n^R\rangle = |\psi_n\rangle \otimes |3\rangle$ satisfies

$$\mathcal{L}|\rho_n^R\rangle = (-iH_{\text{eff}} \otimes I)|\psi_n\rangle \otimes |3\rangle = -iE_n|\rho_n^R\rangle, \quad (44)$$

since $H_{\text{eff}}^*|3\rangle = L_{\mu}^*|3\rangle = 0$. This means that $|\rho_n^R\rangle = |\psi_n\rangle \otimes |3\rangle$ ($\rho_n^R = |\psi_n\rangle\langle 3|$) is an eigenvector (eigenmatrix) of \mathcal{L} (\mathcal{L}) with eigenvalue $-iE_n$. Similarly, one can prove that $|\rho_n^L\rangle = |3\rangle \otimes |\psi_n^*\rangle$ ($\rho_n^L = |3\rangle\langle \psi_n|$) is an eigenvector (eigenmatrix) of \mathcal{L} (\mathcal{L}) with eigenvalue iE_n . The three eigenmatrices $\rho_0^M, \rho_{\pm}^M, \rho_{\mp}^M$ will coalesce into a single density matrix $|\text{EP}\rangle\langle 3|$ for $M=R$ and $|3\rangle\langle \text{EP}|$ for $M=L$, giving rise to a Liouvillian EP3.

While certain Liouvillian EP3 is directly linked to the Hamiltonian EP3 (via the correspondence between eigenstates of H_{eff} and certain eigenmatrices of \mathcal{L}), in the following we show that there exists intrinsic Liouvillian EP3 that do not arise from the eigenstates of the effective Hamiltonian, which can be probed via quench dynamics starting from a non-physical state.

Intrinsic Liouvillian eigenmatrices. We obtain the eigenmatrices and eigenvalues of \mathcal{L} by diagonalizing \mathcal{L} in the doubled Hilbert space (\mathcal{L}), from which we identify intrinsic Liouvillian eigenmatrices that do not arise from the eigenstates of H_{eff} . Specifically, we find three

eigenmatrices written as

$$\rho_{\pm} = \begin{pmatrix} 0 & 1 \pm i\sqrt{\frac{\Omega^2}{\gamma^2} - 1} & i\sqrt{2}\frac{\Omega}{\gamma} & 0 \\ 1 \pm i\sqrt{\frac{\Omega^2}{\gamma^2} - 1} & 0 & 1 \mp i\sqrt{\frac{\Omega^2}{\gamma^2} - 1} & 0 \\ -i\sqrt{2}\frac{\Omega}{\gamma} & 1 \mp i\sqrt{\frac{\Omega^2}{\gamma^2} - 1} & 0 & 0 \\ 0 & 0 & 0 & 0 \end{pmatrix}, \quad (45)$$

$$\rho_0 = \begin{pmatrix} 0 & 1 & i\sqrt{2}\frac{\Omega}{\gamma} & 0 \\ 1 & 0 & 1 & 0 \\ -i\sqrt{2}\frac{\Omega}{\gamma} & 1 & 0 & 0 \\ 0 & 0 & 0 & 0 \end{pmatrix},$$

with the basis being $\{|0\rangle, |1\rangle, |2\rangle, |3\rangle\}$. The corresponding eigenvalues are

$$\lambda_{\pm} = -2\gamma \pm i\sqrt{\Omega^2 - \gamma^2}, \quad (46)$$

$$\lambda_0 = -2\gamma.$$

One can verify that $\mathcal{L}[\rho_n] = \lambda_n \rho_n$ for $n = \pm, 0$. At $\Omega = \gamma$, the eigenvalues become degenerate and the eigenmatrices coalesce into a single density matrix

$$\rho_{\text{EP}} = \begin{pmatrix} 0 & 1 & i\sqrt{2} & 0 \\ 1 & 0 & 1 & 0 \\ -i\sqrt{2} & 1 & 0 & 0 \\ 0 & 0 & 0 & 0 \end{pmatrix}, \quad (47)$$

giving rise to an intrinsic Liouvillian EP3.

We further show that the Liouvillian EP3 emerges from the simultaneous breaking of the PT and anti-PT symmetry, which is the same as the Hamiltonian case. We first prove that the modular conjugation symmetry and an anti-PT symmetry and jump operator structures ensure that eigenvectors of the Lindbladian do not depend on the jump operators. Specifically, the full Lindbladian \mathcal{L} respects the modular conjugation \mathcal{J} ,

$$\mathcal{J}\mathcal{L}\mathcal{J}^{-1} = \mathcal{L}, \quad \mathcal{J}[\rho] = \rho^{\dagger} \quad (48)$$

and the anti-PT symmetry \mathcal{U}_{APT} ,

$$\mathcal{U}_{\text{APT}}\mathcal{L}\mathcal{U}_{\text{APT}}^{-1} = \mathcal{L}, \quad \mathcal{U}_{\text{APT}}[\rho] = \mathcal{U}'_{\text{APT}}\rho(\mathcal{U}'_{\text{APT}})^{-1} \quad (49)$$

with

$$\mathcal{U}'_{\text{APT}} = \begin{pmatrix} 1 & 0 & 0 & 0 \\ 0 & -1 & 0 & 0 \\ 0 & 0 & 1 & 0 \\ 0 & 0 & 0 & 1 \end{pmatrix} \kappa. \quad (50)$$

Since both \mathcal{U}_{APT} and \mathcal{J} are antiunitary symmetries, their combination $\mathcal{U}_{\text{APT}}\mathcal{J}$ is unitary and satisfies $(\mathcal{U}_{\text{APT}}\mathcal{J})^2 = \mathbf{1}$. Thus, if ρ is an eigenvector of \mathcal{L} , then we have

$$(\mathcal{U}_{\text{APT}}\mathcal{J})[\rho] = \mathcal{U}'_{\text{APT}}\rho^{\dagger}(\mathcal{U}'_{\text{APT}})^{-1} = \pm\rho. \quad (51)$$

We focus on the “-” branch since in our case the eigenvectors belong to this branch. Then, ρ takes the following form

$$\rho = \begin{pmatrix} 0 & \rho_{01} & \rho_{02} & \rho_{03} \\ \rho_{01} & 0 & \rho_{12} & \rho_{13} \\ -\rho_{02} & \rho_{12} & 0 & \rho_{23} \\ -\rho_{03} & \rho_{13} & -\rho_{23} & 0 \end{pmatrix}, \quad \rho_{ij} \in \mathbb{C}. \quad (52)$$

Furthermore, in our system the jump operators take the form of $L_\mu = |m_\mu\rangle\langle n_\mu|$ with $m_\mu, n_\mu \in \{0, 1, 2, 3\}$, leading to $L_\mu \rho L_\mu^\dagger = 0$ since symmetries enforce the diagonal elements of ρ to be zero. In this case, ρ is an eigenvector of \mathcal{L} if and only if it is an eigenvector of $\tilde{\mathcal{L}} = -i(H_{\text{eff}} \otimes I - I \otimes H_{\text{eff}}^*)$, or equivalently

$$\tilde{\mathcal{L}}[\cdot] = -iH_{\text{eff}}[\cdot] + i[\cdot]H_{\text{eff}}^*, \quad (53)$$

where H_{eff} is the effective Hamiltonian written in the full Hilbert space, i.e.,

$$H_{\text{eff}} = \begin{pmatrix} 0 & \frac{\Omega}{\sqrt{2}} & 0 & 0 \\ \frac{\Omega}{\sqrt{2}} & -i\gamma & \frac{\Omega}{\sqrt{2}} & 0 \\ 0 & \frac{\Omega}{\sqrt{2}} & -2i\gamma & 0 \\ 0 & 0 & 0 & 0 \end{pmatrix} = \begin{pmatrix} h_{\text{eff}} - i\gamma I_3 & \mathbf{0} \\ \mathbf{0} & 0 \end{pmatrix}. \quad (54)$$

Based on the structure of H_{eff} ,

$$\tilde{\rho} = \begin{pmatrix} \rho_{00} & \rho_{01} & \rho_{02} & 0 \\ \rho_{10} & \rho_{11} & \rho_{12} & 0 \\ \rho_{20} & \rho_{21} & \rho_{22} & 0 \\ 0 & 0 & 0 & 0 \end{pmatrix} \quad (55)$$

is an eigenvector of $\tilde{\mathcal{L}}$ with eigenvalue λ if and only if

$$\rho_{\text{sys}} = \begin{pmatrix} \rho_{00} & \rho_{01} & \rho_{02} \\ \rho_{10} & \rho_{11} & \rho_{12} \\ \rho_{20} & \rho_{21} & \rho_{22} \end{pmatrix} \quad (56)$$

is an eigenvector of

$$\mathcal{L}_{\text{sys}} = -i(h_{\text{eff}} \otimes I_3 - I_3 \otimes h_{\text{eff}}^*) \quad (57)$$

with eigenvalue $\lambda + 2\gamma$. This allows us to set $\rho_{i3} = \rho_{3i} = 0$ for $i = 0, 1, 2, 3$ so that

$$\rho = \begin{pmatrix} 0 & \rho_{01} & \rho_{02} & 0 \\ \rho_{01} & 0 & \rho_{12} & 0 \\ -\rho_{02} & \rho_{12} & 0 & 0 \\ 0 & 0 & 0 & 0 \end{pmatrix}. \quad (58)$$

Since h_{eff} respects both the PT symmetry and the anti-PT symmetry, we have

$$\begin{aligned} (U_{\text{PT}} \otimes U_{\text{PT}}^*) \mathcal{L}_{\text{sys}} (U_{\text{PT}} \otimes U_{\text{PT}}^*)^{-1} &= -\mathcal{L}_{\text{sys}}, \\ (U_{\text{APT}} \otimes U_{\text{APT}}^*) \mathcal{L}_{\text{sys}} (U_{\text{APT}} \otimes U_{\text{APT}}^*)^{-1} &= \mathcal{L}_{\text{sys}}. \end{aligned} \quad (59)$$

We thus see that the PT symmetry represented by $U_{\text{PT}} \otimes U_{\text{PT}}^*$ and the anti-PT symmetry represented by $U_{\text{APT}} \otimes U_{\text{APT}}^*$ ensure the existence of EP3 in \mathcal{L}_{sys} (thus \mathcal{L}) as the two symmetries break at the same parameter value as in the Hamiltonian case. For the winding topology of a Liouvillian EP3, see the discussion in Supplementary Information S-4.

Detection of the intrinsic Liouvillian EP3. To detect the EP3 associated with PT symmetry breaking, we adopt an initial state that can be written as a linear combination of the three eigenmatrices. We define

$$\begin{aligned} |u_1\rangle &= \frac{1}{\sqrt{2}}(|0\rangle - i|2\rangle) = \frac{1}{\sqrt{2}}(1 \ 0 \ -i \ 0)^T, \\ |u_2\rangle &= \frac{1}{\sqrt{2}}(|0\rangle + i|2\rangle) = \frac{1}{\sqrt{2}}(1 \ 0 \ i \ 0)^T. \end{aligned} \quad (60)$$

The initial state is chosen as

$$\begin{aligned} \rho(0) &= |u_1\rangle\langle u_1| - |u_2\rangle\langle u_2| \\ &= \frac{\Omega\gamma}{\sqrt{2}(\gamma^2 - \Omega^2)} [\rho_0 - \frac{1}{2}(\rho_+ + \rho_-)]. \end{aligned} \quad (61)$$

The time evolution of $\rho(0)$ is then given by

$$\begin{aligned} \rho(t) &= e^{\mathcal{L}t}[\rho(0)] \\ &= \frac{\Omega\gamma}{\sqrt{2}(\gamma^2 - \Omega^2)} [e^{\lambda_0 t} \rho_0 - \frac{1}{2}(e^{\lambda_+ t} \rho_+ + e^{\lambda_- t} \rho_-)] \\ &= \frac{\Omega\gamma}{\sqrt{2}(\gamma^2 - \Omega^2)} e^{-2\gamma t} \begin{pmatrix} 0 & A(t) & C(t) & 0 \\ A^*(t) & 0 & B(t) & 0 \\ C^*(t) & B^*(t) & 0 & 0 \\ 0 & 0 & 0 & 0 \end{pmatrix}, \end{aligned} \quad (62)$$

where

$$\begin{aligned} A(t) &= 1 - \cos(\sqrt{\Omega^2 - \gamma^2}t) + \sqrt{\frac{\Omega^2}{\gamma^2} - 1} \sin(\sqrt{\Omega^2 - \gamma^2}t), \\ B(t) &= 1 - \cos(\sqrt{\Omega^2 - \gamma^2}t) - \sqrt{\frac{\Omega^2}{\gamma^2} - 1} \sin(\sqrt{\Omega^2 - \gamma^2}t), \\ C(t) &= -\frac{i\sqrt{2}}{\Omega\gamma} [\Omega^2 \cos(\sqrt{\Omega^2 - \gamma^2}t) - \gamma^2]. \end{aligned} \quad (63)$$

From Eq. (62) and Eq. (63), we find

$$\rho_{12}(t) - \rho_{01}(t) = \frac{\sqrt{2}\Omega}{\sqrt{\Omega^2 - \gamma^2}} e^{-2\gamma t} \sin(\sqrt{\Omega^2 - \gamma^2}t), \quad (64)$$

which can be used to detect the PT phase transition.

Since $\text{Tr}[\rho(0)] = 0$, the state $\rho(0)$ cannot be directly prepared as it is not a physical state. To address this, we define

$$\begin{aligned} \sigma(0) &= |u_1\rangle\langle u_1|, \quad \sigma(t) = e^{\mathcal{L}t}[|u_1\rangle\langle u_1|], \\ \tau(0) &= |u_2\rangle\langle u_2|, \quad \tau(t) = e^{\mathcal{L}t}[|u_2\rangle\langle u_2|]. \end{aligned} \quad (65)$$

Experimentally, we can prepare the states $|u_1\rangle$ and $|u_2\rangle$, measure the matrix elements of $\sigma(t)$ and $\tau(t)$, respectively, and then obtain $\rho(t)$ using the relation $\rho(t) = \sigma(t) - \tau(t)$ (see Supplementary Information S-5 for the generic case). Furthermore, due to the anti-PT symmetry of the system, we have

$$\begin{aligned} \tau_{01}(t) &= -\sigma_{01}^*(t), \\ \tau_{12}(t) &= -\sigma_{12}^*(t). \end{aligned} \quad (66)$$

This allows us to express

$$\rho_{12}(t) - \rho_{01}(t) = 2\text{Re}(\sigma_{12}(t) - \sigma_{01}(t)), \quad (67)$$

which means that we only need to prepare $|u_1\rangle$ and measure the off-diagonal elements of $\sigma(t)$.

The proof of Eq. (66) is as follows. The anti-PT symmetry of the Lindbladian gives rise to the relation

$$U'_{\text{APT}} \mathcal{L}[\sigma(t)] (U'_{\text{APT}})^{-1} = \mathcal{L}[U'_{\text{APT}} \sigma(t) (U'_{\text{APT}})^{-1}], \quad (68)$$

which implies that

$$U'_{\text{APT}} e^{\mathcal{L}t} [\sigma(0)] (U'_{\text{APT}})^{-1} = e^{\mathcal{L}t} [U'_{\text{APT}} \sigma(0) (U'_{\text{APT}})^{-1}]. \quad (69)$$

Since $\tau(0) = U'_{\text{APT}} \sigma(0) (U'_{\text{APT}})^{-1}$, Eq. (69) gives rise to the relation

$$\tau(t) = U'_{\text{APT}} \sigma(t) (U'_{\text{APT}})^{-1}, \quad (70)$$

which leads to Eq. (66).

Data availability

The data that support the findings of this study are available at Figshare <https://doi.org/10.6084/m9.figshare.29301071> (ref. 67).

References

- Bender, C. M. & Boettcher, S. Real spectra in non-hermitian hamiltonians having \mathcal{PT} symmetry. *Phys. Rev. Lett.* **80**, 5243 (1998).
- Bender, C. M. Making sense of non-Hermitian Hamiltonians. *Rep. Prog. Phys.* **70**, 947 (2007).
- Christodoulides, D. et al. *Parity-time symmetry and its applications*. (Springer, 2018).
- Heiss, W. D. Exceptional points of non-Hermitian operators. *J. Phys. A Math. Gen.* **37**, 2455 (2004).
- Berry, M. Physics of Nonhermitian Degeneracies. *Czech. J. Phys.* **54**, 1039 (2004).
- El-Ganainy, R. et al. Non-Hermitian physics and PT symmetry. *Nat. Phys.* **14**, 11 (2018).
- Xu, Y. Topological gapless matters in three-dimensional ultracold atomic gases. *Front. Phys.* **14**, 43402 (2019).
- Ashida, Y., Gong, Z. & Ueda, M. Non-Hermitian physics. *Adv. Phys.* **69**, 249 (2020).
- Domínguez-Rocha, V., Thevamaran, R., Ellis, F. & Kottos, T. Environmentally induced exceptional points in elastodynamics. *Phys. Rev. Appl.* **13**, 014060 (2020).
- Bergholtz, E. J., Budich, J. C. & Kunst, F. K. Exceptional topology of non-hermitian systems. *Rev. Mod. Phys.* **93**, 015005 (2021).
- Ding, K., Fang, C. & Ma, G. Non-Hermitian topology and exceptional-point geometries. *Nat. Rev. Phys.* **4**, 745 (2022).
- Quiroz-Juárez, M. A. et al. On-demand parity-time symmetry in a lone oscillator through complex synthetic gauge fields. *Phys. Rev. Appl.* **18**, 054034 (2022).
- Feng, L., Wong, Z. J., Ma, R.-M., Wang, Y. & Zhang, X. Single-mode laser by parity-time symmetry breaking. *Science* **346**, 972 (2014).
- Hodaie, H., Miri, M.-A., Heinrich, M., Christodoulides, D. N. & Khajavikhan, M. Parity-time-symmetric microring lasers. *Science* **346**, 975 (2014).
- Moiseyev, N. *Non-Hermitian Quantum Mechanics*. (Cambridge University Press, Cambridge, England, 2011).
- Lee, S.-B. et al. Observation of an exceptional point in a chaotic optical microcavity. *Phys. Rev. Lett.* **103**, 134101 (2009).
- Rüter, C. E. et al. Observation of parity-time symmetry in optics. *Nat. Phys.* **6**, 192 (2010).
- Zhen, B. et al. Spawning rings of exceptional points out of Dirac cones. *Nature* **525**, 354 (2015).
- Xu, Y., Wang, S.-T. & Duan, L.-M. Weyl exceptional rings in a three-dimensional dissipative cold atomic gas. *Phys. Rev. Lett.* **118**, 045701 (2017).
- Cerjan, A. et al. Experimental realization of a Weyl exceptional ring. *Nat. Photonics* **13**, 623 (2019).
- Carlström, J., Stålhammar, M., Budich, J. C. & Bergholtz, E. J. Knotted non-hermitian metals. *Phys. Rev. B* **99**, 161115 (2019).
- Stålhammar, M., Rørdland, L., Arone, G., Budich, J. C. & Bergholtz, E. Hyperbolic nodal band structures and knot invariants. *SciPost Phys.* **7**, 019 (2019).
- Hou, J., Li, Z., Luo, X.-W., Gu, Q. & Zhang, C. Topological bands and triply degenerate points in non-hermitian hyperbolic metamaterials. *Phys. Rev. Lett.* **124**, 073603 (2020).
- Yang, Z., Chiu, C.-K., Fang, C. & Hu, J. Jones polynomial and knot transitions in hermitian and non-hermitian topological semimetals. *Phys. Rev. Lett.* **124**, 186402 (2020).
- Chen, W., Kaya Özdemir, Ş., Zhao, G., Wiersig, J. & Yang, L. Exceptional points enhance sensing in an optical microcavity. *Nature* **548**, 192 (2017).
- Lin, Z. et al. Unidirectional invisibility induced by \mathcal{PT} -symmetric periodic structures. *Phys. Rev. Lett.* **106**, 213901 (2011).
- Wu, Y. et al. Observation of parity-time symmetry breaking in a single-spin system. *Science* **364**, 878 (2019).
- Li, J. et al. Observation of parity-time symmetry breaking transitions in a dissipative Floquet system of ultracold atoms. *Nat. Commun.* **10**, 855 (2019).
- Naghiloo, M., Abbasi, M., Joglekar, Y. N. & Murch, K. W. Quantum state tomography across the exceptional point in a single dissipative qubit. *Nat. Phys.* **15**, 1232 (2019).
- Partanen, M. et al. Exceptional points in tunable superconducting resonators. *Phys. Rev. B* **100**, 134505 (2019).
- Ding, L. et al. Experimental determination of \mathcal{PT} -symmetric exceptional points in a single trapped ion. *Phys. Rev. Lett.* **126**, 083604 (2021).
- Wang, W.-C. et al. Observation of \mathcal{PT} -symmetric quantum coherence in a single-ion system. *Phys. Rev. A* **103**, L020201 (2021).
- Liu, W., Wu, Y., Duan, C.-K., Rong, X. & Du, J. Dynamically encircling an exceptional point in a real quantum system. *Phys. Rev. Lett.* **126**, 170506 (2021).
- Zhang, W. et al. Observation of non-hermitian topology with non-unitary dynamics of solid-state spins. *Phys. Rev. Lett.* **127**, 090501 (2021).
- Ren, Z. et al. Chiral control of quantum states in non-Hermitian spin-orbit-coupled fermions. *Nat. Phys.* **18**, 385 (2022).
- Yu, Y. et al. Experimental unsupervised learning of non-Hermitian knotted phases with solid-state spins. *Npj Quantum Inf.* **8**, 116 (2022).
- Heiss, W. D. Chirality of wavefunctions for three coalescing levels. *J. Phys. A Math. Theor.* **41**, 244010 (2008).
- Demange, G. & Graefe, E.-M. Signatures of three coalescing eigenfunctions. *J. Phys. A Math. Theor.* **45**, 025303 (2012).
- Hodaie, H. et al. Enhanced sensitivity at higher-order exceptional points. *Nature* **548**, 187 (2017).
- Tang, W. et al. Exceptional nexus with a hybrid topological invariant. *Science* **370**, 1077 (2020).
- Wang, K. et al. Experimental simulation of symmetry-protected higher-order exceptional points with single photons. *Sci. Adv.* **9**, eadi0732 (2023).
- Wang, K. et al. Photonic Non-Abelian Braid Monopole. Preprint at <https://arxiv.org/abs/2410.08191> (2024).
- Wang, C. et al. Exceptional nexus in bose-einstein condensates with collective dissipation. *Phys. Rev. Lett.* **132**, 253401 (2024).
- Günther, U. & Samsonov, B. F. Naimark-dilated pt-symmetric brachistochrone. *Phys. Rev. Lett.* **101**, 230404 (2008).
- Kawabata, K., Ashida, Y. & Ueda, M. Information retrieval and criticality in parity-time-symmetric systems. *Phys. Rev. Lett.* **119**, 190401 (2017).
- Wu, Y. et al. Third-order exceptional line in a nitrogen-vacancy spin system. *Nat. Nanotechnol.* **19**, 160 (2024).

47. Liang, C., Tang, Y., Xu, A.-N. & Liu, Y.-C. Observation of exceptional points in thermal atomic ensembles. *Phys. Rev. Lett.* **130**, 263601 (2023).
 48. Chen, W. et al. Decoherence-induced exceptional points in a dissipative superconducting qubit. *Phys. Rev. Lett.* **128**, 110402 (2022).
 49. Cao, M.-M. et al. Probing complex-energy topology via non-hermitian absorption spectroscopy in a trapped ion simulator. *Phys. Rev. Lett.* **130**, 163001 (2023).
 50. Li, K. & Xu, Y. Non-hermitian absorption spectroscopy. *Phys. Rev. Lett.* **129**, 093001 (2022).
 51. Olmschenk, S. et al. Measurement of the lifetime of the $6p^2P_{1/2}^o$ level of yb^+ . *Phys. Rev. A* **80**, 022502 (2009).
 52. Delplace, P., Yoshida, T. & Hatsugai, Y. Symmetry-protected multi-fold exceptional points and their topological characterization. *Phys. Rev. Lett.* **127**, 186602 (2021).
 53. Mandal, I. & Bergholtz, E. J. Symmetry and higher-order exceptional points. *Phys. Rev. Lett.* **127**, 186601 (2021).
 54. Zeng, Q.-B., Yang, Y.-B. & Xu, Y. Topological phases in non-hermitian Aubry-André-Harper models. *Phys. Rev. B* **101**, 020201 (2020).
 55. Minganti, F., Miranowicz, A., Chhajlany, R. W. & Nori, F. Quantum exceptional points of non-Hermitian Hamiltonians and Liouvillians: The effects of quantum jumps. *Phys. Rev. A* **100**, 062131 (2019).
 56. Chen, W., Abbasi, M., Joglekar, Y. N. & Murch, K. W. Quantum jumps in the non-hermitian dynamics of a superconducting qubit. *Phys. Rev. Lett.* **127**, 140504 (2021).
 57. Zhang, J.-W. et al. Dynamical control of quantum heat engines using exceptional points. *Nat. Commun.* **13**, 6225 (2022).
 58. Bu, J.-T. et al. Enhancement of quantum heat engine by encircling a Liouvillian exceptional point. *Phys. Rev. Lett.* **130**, 110402 (2023).
 59. Hu, H. & Zhao, E. Knots and non-hermitian Bloch bands. *Phys. Rev. Lett.* **126**, 010401 (2021).
 60. Wojcik, C. C., Wang, K., Dutt, A., Zhong, J. & Fan, S. Eigenvalue topology of non-hermitian band structures in two and three dimensions. *Phys. Rev. B* **106**, L161401 (2022).
 61. Verstraete, F., Wolf, M. M. & Ignacio Cirac, J. Quantum computation and quantum-state engineering driven by dissipation. *Nat. Phys.* **5**, 633 (2009).
 62. Altman, E. et al. Quantum simulators: Architectures and opportunities. *PRX quantum* **2**, 017003 (2021).
 63. Li, Y. et al. Programmable simulation of high-order exceptional point with a trapped ion. <https://arxiv.org/abs/2412.09776> (2024).
 64. Tan, T., Edmunds, C., Milne, A., Biercuk, M. & Hempel, C. Precision characterization of the $d\ 5/2\ 2$ state and the quadratic Zeeman coefficient in yb^+ 171. *Phys. Rev. A* **104**, L010802 (2021).
 65. Jamiolkowski, A. Linear transformations which preserve trace and positive semidefiniteness of operators. *Rep. Math. Phys.* **3**, 275 (1972).
 66. Choi, M.-D. Completely positive linear maps on complex matrices. *Linear Algebra Appl.* **10**, 285 (1975).
 67. Chen, Y.-Y. et al. Data supporting our work “Quantum tomography of a third-order exceptional point in a dissipative trapped ion”. Figshare <https://doi.org/10.6084/m9.figshare.29301071> (2025).
- discussions. This work was supported by the Innovation Program for Quantum Science and Technology (grant nos. 2021ZD0301601 and 2021ZD0301604), the Shanghai Qi Zhi Institute, Tsinghua University Initiative Scientific Research Program, and the Ministry of Education of China. L.M.D. acknowledges, in addition, support from the New Cornerstone Science Foundation through the New Cornerstone Investigator Program. Y.X. acknowledges in addition support from the National Natural Science Foundation of China (Grants No. 12474265 and No. 11974201). Y.K.W. acknowledges in addition support from the Tsinghua University Dushi program. P.Y.H. acknowledges support from the Tsinghua University Dushi Program and the Tsinghua University Start-up Fund.

Author contributions

Y.X. proposed the idea. Y.Y.C., L.Z., J.Y.M., H.X.Y., C.Z., B.X.Q., Z.C.Z., and P.Y.H. carried out the experiment. K.L., Y.X., and Y.K.W. developed the associated theory. L.M.D. supervised the project.

Competing interests

The authors declare that there are no competing interests.

Additional information

Supplementary information The online version contains supplementary material available at <https://doi.org/10.1038/s41467-025-62573-5>.

Correspondence and requests for materials should be addressed to P.-Y. Hou, Y. Xu or L.-M. Duan.

Peer review information *Nature Communications* thanks Weijian Chen, and the other anonymous reviewers for their contribution to the peer review of this work. A peer review file is available.

Reprints and permissions information is available at <http://www.nature.com/reprints>

Publisher's note Springer Nature remains neutral with regard to jurisdictional claims in published maps and institutional affiliations.

Open Access This article is licensed under a Creative Commons Attribution-NonCommercial-NoDerivatives 4.0 International License, which permits any non-commercial use, sharing, distribution and reproduction in any medium or format, as long as you give appropriate credit to the original author(s) and the source, provide a link to the Creative Commons licence, and indicate if you modified the licensed material. You do not have permission under this licence to share adapted material derived from this article or parts of it. The images or other third party material in this article are included in the article's Creative Commons licence, unless indicated otherwise in a credit line to the material. If material is not included in the article's Creative Commons licence and your intended use is not permitted by statutory regulation or exceeds the permitted use, you will need to obtain permission directly from the copyright holder. To view a copy of this licence, visit <http://creativecommons.org/licenses/by-nc-nd/4.0/>.

© The Author(s) 2025

Acknowledgements

We thank Mingming Cao, Wending Zhao, Shi-An Guo, Ye Jin, Li You, Wei Yi, Xun Gao, Masahito Ueda, and Yan-Bin Yang for helpful